

# A Method for Spatial Quantification of Water in Microporous Layers of Polymer Electrolyte Fuel Cells by X-ray Tomographic Microscopy

Yen-Chun Chen, Anne Berger, Salvatore De Angelis, Tobias Schuler, Michele Bozzetti, Jens Eller, Vasiliki Tileli, Thomas J. Schmidt, and Felix N. Büchi\*



Cite This: *ACS Appl. Mater. Interfaces* 2021, 13, 16227–16237



Read Online

ACCESS |



Metrics & More



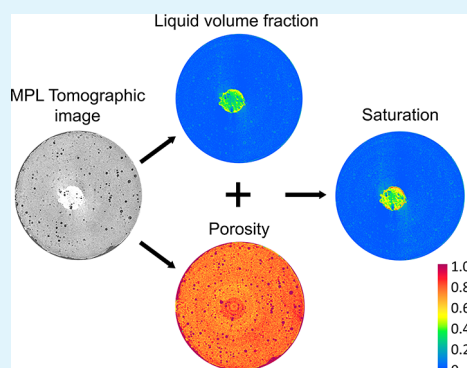
Article Recommendations



Supporting Information

**ABSTRACT:** A microporous layer (MPL) is typically added to the gas diffusion layer of polymer electrolyte fuel cells (PEFCs) to promote cell performance and water management. The transport mechanism of the water through the MPL is, however, not well understood due to its small pores (20–500 nm). Here, we demonstrate that polychromatic X-ray tomographic microscopy (XTM) can be used to determine the porosity and the spatial distribution of water in nanoporous materials and can quantitatively map the liquid water saturation of MPLs. The presented technique requires no a priori knowledge of the composition of the MPL and has a field of view on the millimeter scale, which is orders of magnitude larger than conventional electron microscopy techniques for nanoscale materials. The available field of view is compatible with existing operando cells for X-ray tomography, paving the way for the analysis of water transport in MPLs during operation.

**KEYWORDS:** polymer electrolyte fuel cells, microporous layer, X-ray tomographic microscopy, local porosity determination, liquid water distribution, water management, subvoxel imaging



## INTRODUCTION

The increasing emission of greenhouse gases (GHGs) and the associated global warming are imminent issues. About one-quarter of the global CO<sub>2</sub> emission comes from the transportation sector alone.<sup>1</sup> There, hydrogen is considered to be a promising energy carrier.<sup>2,3</sup>

For transportation applications, hydrogen is converted to electric power in polymer electrolyte fuel cells (PEFCs) where water accumulates in the cathode gas diffusion layer (GDL) in particular during operation at high current densities. Water saturation in the GDL leads to constricted oxygen transport from the gas channels to the catalyst layer,<sup>4,5</sup> limiting the cell performance.<sup>6</sup> As a result, peak power or efficiency at high power density is limited, which effectively hinders the cost reduction for the fuel cell systems. The latter is one of the major barriers to general market adoption.

For optimizing fuel cell performance, it is a standard to add a microporous layer (MPL) between the catalyst layer (CL) and the gas diffusion layer to improve water management.<sup>7–11</sup> MPLs, with thicknesses of about 20–50 μm, are made of nanoscale carbon particles bound by fluoropolymer binders,<sup>12,13</sup> resulting in a porous structure with average pore sizes in the range of 20 to 500 nm.<sup>14</sup> The addition of a microporous layer reduces the water saturation in the GDL, leaving more pathways for oxygen transport at the cathode.<sup>15–17</sup> Furthermore, it has been shown that MPLs reduce electrical resistance in the cell<sup>14</sup> and increase the mechanical integrity of the

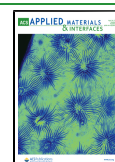
GDL.<sup>18</sup> MPLs also prevent the carbon fibers of the GDL from damaging the catalyst layer and the membrane upon direct contact.<sup>19</sup> However, the details on the water transport mechanisms inside the MPL are not clear. Different mechanistic explanations are proposed.

Deevanhxay et al.,<sup>20</sup> Oberholzer et al.,<sup>21</sup> and Owejan et al.<sup>22</sup> argued that the MPL improves performance by reducing water flooding at the catalyst layer. Baghalha,<sup>23</sup> Weber and Newman,<sup>24</sup> Wang and Nguyen,<sup>25</sup> and Kim et al.,<sup>26</sup> on the other hand, proposed that the performance enhancement benefits from the back-transport of water from the cathode toward the membrane when an MPL capillary barrier is introduced. Furthermore, it has been shown that liquid water selectively passes through the bigger pores of the MPL, establishing preferential pathways with subsequent reduction of the water accumulation in the GDL,<sup>15,27</sup> and some argued that the intrusion of the MPL into the GDL effectively provides direct pathways via the cracks, reducing the chances for capillary fingering (high saturation patterns) before breakthrough.<sup>28</sup> It is expected that direct imaging of the

**Received:** December 17, 2020

**Accepted:** February 10, 2021

**Published:** March 16, 2021



water in the MPL provides important information for understanding how MPLs improve water transport, and design guidelines for further improved MPL structures can be deduced.

Nam et al. used environmental scanning electron microscopy (ESEM) to visualize water condensation on the surface of the MPL.<sup>29</sup> The field of view was a few hundreds of micrometers; however, the mesopores of the MPL were not clearly resolved, and the method was unable to characterize water inside the MPL pores. Aoyama et al. pushed the resolution forward and used *ex situ* cryo-scanning electron microscopy (cryo-SEM) to image water (in the form of ice) in the pores of the MPL in a postmortem, frozen state. The water was seen in the MPL pores, but the field of view was confined to the micrometer scale; the characterization required freezing and disassembling of the fuel cell and could not be performed operando.<sup>30</sup> Fishman and Bazylak visually characterized the cracks and holes of the MPL, accounting for the porosity contribution from these features by laboratory X-ray computed tomography.<sup>31</sup> Halter et al. used synchrotron-based, operando X-ray tomographic microscopy (XTM) to quantify the temporal evolution of the progression of phosphoric acid into the MPL cracks in high-temperature polymer electrolyte fuel cells.<sup>32</sup> Both techniques pushed the characterization of liquid toward the inside of the MPL. However, the existence of liquid (water or phosphoric acid) in the primary pores of the MPL was not addressed. Recently, Kato et al. qualitatively distinguished the wet domains of the MPL from the dry domains in an *ex situ* water condensation experiment using synchrotron-based X-ray computed tomography.<sup>33</sup> Akitomo et al. quantitatively determined the water content in the MPL at various cell operating conditions via X-ray radiography, enabling further understanding of the influence of the 2D water accumulation in the MPL at different cell operating conditions.<sup>34</sup> These are some of the few results that provided the visualization of water in the MPL's primary pores, together with the work of Alwashdeh et al. The latter had characterized the wet domain of the MPL in an operando fuel cell by synchrotron X-ray *phase contrast* tomography.<sup>35</sup> However, the reported results were more qualitative than quantitative.

Until now, there has not been a quantitative description of the 3D water saturation in the MPL with a representative field of view that spans across the repetitive channel-rib structure ( $\gg 2 \text{ mm}^2$ <sup>36</sup>), which is relevant to fuel cell operation. The main difficulty lies in the incompatibility of the sufficiently powerful nanoscale imaging techniques with liquid water due to high vacuum environment requirements or long acquisition times (e.g., SEM, nanoscale X-ray computed tomography, and focused ion beam scanning electron microscopy). Furthermore, another challenge is the low water content associated with the wet domains of the MPL requiring highly sensitive methods.

With the ability to house a fully operational fuel cell and to obtain three-dimensional volume renderings of structural features and the realization of fast operando measurements,<sup>37–40</sup> X-ray tomographic microscopy (XTM) is considered a promising technique for understanding water transport in the MPL as well. The present work is performed using a laboratory computed tomography (CT) scanner for method development due to the possibility of performing longer tests without limitations from the availability of synchrotron beamtime. We show that, by analyzing and calibrating the grayscale values (GSVs) of the XTM images,

the water saturation in the microporous layer can be derived quantitatively with polychromatic X-ray radiation at micrometer-scale resolution. Understanding the MPL saturation is crucial, as it plays a key role in the permeability and relative effective diffusivity in the porous transport layers.<sup>41–43</sup> The millimeter-scale field of view bridges the gap between the nanoscale microporous layer pore description and the macroscale fuel cell performance evaluation. The ability to use a polychromatic X-ray source allows for operando laboratory-scale measurements, broadening the applicability of this technique. In this work, the method is also validated for nanoporous model materials using an organic wetting liquid, demonstrating its applicability to other systems and problems.

## EXPERIMENTAL SECTION

**Materials. Sample Holder.** A cylindrical sample holder made of polyether–ether–ketone (PEEK) was used for X-ray tomographic image acquisition. It is equipped with an adjustable compression screw and a closing piece that allows for compression of the samples positioned in the sample chamber. The outer diameter of the housing unit is 10 mm, and the inner diameter is 7.5 mm. The sample chamber allows horizontal placement of sample disks of up to 7 mm in diameter. The housing unit is an open system having an injection bore from the bottom of the sample chamber and an air outlet bore that goes through the closing piece and the compression screw. The liquid is injected by a syringe pump connected by a tube (Festo; type: PUN-H-3  $\times$  0.5 NT) to the bottom bore during the wetting procedure, while compression can be applied by turning the adjustable screw. A schematic illustration of the compartments of the sample holder is shown in Figure 1.

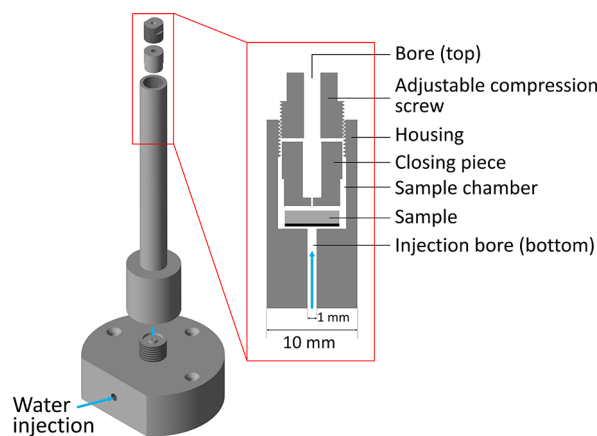


**Figure 1.** Schematic drawing of the cylindrical sample holder with an adjustable compression screw, all made of PEEK, for X-ray tomographic microscopy.

**Membrane Filters as Model Materials.** Durapore PVDF biological membrane filters GVWP04700, HVHP04700, and DVPP04700 (Merck Millipore Ltd.) were used as model materials because they have pore size distributions and porosity values similar to those of a typical MPL. The hydrophilic ones are denoted as H22 (for GVWP04700 with 0.22  $\mu\text{m}$  average pore size) and H65 (for DVPP04700 with 0.65  $\mu\text{m}$  pore size). The hydrophobic one, HVHP04700, has an average pore size of 0.45  $\mu\text{m}$  and is denoted as P45. The initial porosity was measured by comparing the dry weight and the liquid-saturated weight of liquids with known densities at 25  $^\circ\text{C}$  (*n*-decane and water) and determined to be  $66 \pm 0.8\%$ ,  $64 \pm 1\%$ , and  $59 \pm 1.4\%$  for H22, H65, and P45, respectively. The details of the measurement are given Section S1.1.

**Commercial MPL.** The Freudenberg H23C6 carbon paper gas diffusion layer (GDL) with a smooth, crack-free microporous layer

(bought from Quintech, Germany) was used as the commercially available material.

**In-House Made MPL.** The “Li100 MPL” was prepared on a commercially available PTFE-treated Freudenberg H14 gas diffusion layer substrate as described by Simon et al. (and henceforth referred to as Li100/H14). The MPL consists of acetylene black (Denka black Li100) and 20 wt % PTFE binder. Its structural properties are well documented and therefore served as a well-defined MPL with 80% porosity as previously measured by mercury intrusion porosimetry (MIP). The manufacturing process and structural characterizations are described in detail in ref 44.

**Vapor-Grown Carbon Fiber MPL.** The vapor-grown carbon fiber (VGCF) MPL was prepared on a commercially available PTFE-treated Freudenberg H14 GDL substrate (thus denoted as VGCF/H14). The MPL uses vapor-grown carbon fibers, VGCF-H (Showa Denko; fiber diameter = 150 nm), as the carbon component and PTFE (58 wt % PTFE dispersion TF 5035GZ from 3 M Dyneon) as the hydrophobic binder. The thickness of the MPL was increased in comparison to the common fuel cell operation for imaging purposes. The detailed manufacturing procedure is described by Simon et al.<sup>27,44</sup> The final VGCF MPL is hydrophobic with a PTFE content of 20 wt % and has 83% porosity measured by mercury intrusion porosimetry.

**Wetting Liquids.** *N*-Decane and ethanol absolute (≥99.8%) were bought from Thermo Fisher/Fisher Scientific AG (Switzerland) and Merck KGaA (Germany), respectively, and are used for achieving complete saturation of the MPLs and model materials. Deionized water (380 ± 50 kΩ cm) was used whenever water is mentioned.

**XTM Imaging.** A CT scanner phoenix nanotom m (General Electric, Germany) with a Phoenix X-ray tube was used for all tomographic data. For all scans, the acquisition parameters are the same. For X-ray generation, 60 kV acceleration voltage and 200 μA current were set. Each radiographic projection was taken by averaging 3 consecutive projections and skipping 1 following projection. A total of 2400 projections were acquired for the reconstruction of high-quality images. During the scan, local tomography was duly avoided to ensure that the grayscale values (32-bit floating point) remain quantitative across scans. Detector calibration was performed before every tomographic scan, and a radiographic region of constant air phase was selected as “observational ROI” to calibrate X-ray flux fluctuation during the scan. A voxel edge length between 2.5 and 3.6 μm was used. The settings resulted in a typical acquisition time of about 80 min.

**Compressed Porosity and Liquid Saturation.** Compression of the model materials H22 and H65 was set manually by decreasing the chamber height with the adjustable screw from the top of the sample holder. The original thickness ( $d_0$ ) was measured by a digital indicator, MarCator 1075 R (Mahr, Germany), and the exact compressed thickness ( $d$ ) was evaluated from the tomographic images. More details are provided in Section S1.2. The compression ratio was calculated according to  $(d_0 - d)/d_0$ . The compressed porosity of the model materials, assuming that the solid part is incompressible and the samples are homogeneous, is calculated as

$$\varepsilon = 1 - \frac{d_0}{d}(1 - \varepsilon_0) \quad (1)$$

In eq 1,  $\varepsilon_0$  is the initial porosity value of the membrane filter from the gravimetric measurements (Section S1.1).

Saturation of an MPL or a compressed model material is achieved by filling the sample with an excessive amount of the wetting liquid from the bottom injection bore of the cylindrical housing unit and is followed by immersion within the wetting liquid for 30 min.

**Water-Wetting of the Microporous Layer.** The wetting of the VGCF MPL with water was performed manually by injecting the water with a syringe from the bottom injection bore until excess water flowed out of the sample holder from the top air outlet bore. The MPL side of the VGCF/H14 directly faced the bottom injection bore to ensure water imbibition via the MPL pores.

**Image Evaluation Methodology.** *Quantitative X-ray Tomographic Imaging with Polychromatic Radiation.* When using a

monochromatic X-ray source, the tomographic reconstructed grayscale values (GSVs) are proportional to the linear attenuation coefficient at each voxel. In other words,

$$GSV(\vec{r}, E) \propto \sum_i^n \mu_{\text{mass},i}(Z, E) \rho_i V_i(\vec{r}) = \sum_i^n \mu_i(\rho, V, Z, E, \vec{r}) \quad (2)$$

where  $\mu_{\text{mass},i}$  and  $\mu_i$  are the mass and linear attenuation coefficients of the  $i^{\text{th}}$  material phase in the voxel located at  $\vec{r}$ , respectively.  $\rho_i$  is the mass density of the  $i^{\text{th}}$  phase, and  $V_i$  is the volume fraction occupied by the  $i^{\text{th}}$  phase in the voxel.  $Z$  is the atomic number.  $E$  is the X-ray energy, and  $n$  is the number of phases present in that voxel at  $\vec{r}$ .

When the X-ray is polychromatic, however, the energy-dependent attenuation coefficients of the materials are not straightforwardly defined. As a result, the mass density of the materials can no longer be derived easily from the grayscale values. This occurs when a white beam at the synchrotron radiation facility or a laboratory X-ray CT scanner is used. Under such circumstances, the reconstructed grayscale values are usually only analyzed qualitatively. Nonetheless, White et al. used a low-energy X-ray filter to narrow the X-ray energy distribution of the laboratory CT scanner and showed that a monochromatic light source assumption could approximately hold for the remaining X-ray radiation, and the tomographic imaging results were regarded as quantitative.<sup>45</sup>

Here, we also show that the GSV obtained by the polychromatic lab CT can be used to derive material mass density. The grayscale values of air, *n*-decane, ethanol, water, PEEK, pyrolytic graphite (Union Carbide, USA), and PTFE are first obtained with a fixed set of X-ray tube parameters as previously mentioned (60 kV acceleration voltage, 200 μA electron current). These material phases are inspected because they are relevant to the composition of a typical MPL and to the liquids involved in this experiment. The GSVs are then compared to the linear attenuation coefficients of each material phase at a specific energy between 1 and 60 keV using the values from the NIST database.<sup>46,47</sup> A MATLAB script is used to iteratively examine the linearity between the grayscale values and the attenuation coefficients, returning the  $R^2$  value at each energy. The  $R^2$  values for each X-ray energy from 1 to 60 keV (for which the linear attenuation coefficients were returned) are plotted in Figure 2a. At 34.3 keV,  $R^2$  peaks and is close to unity (0.998); therefore, the laboratory CT scanner produces GSVs that are proportional to the linear attenuation coefficients of the selected materials at this energy. The relationship is plotted in Figure 2b.

It does not entail that the lab CT produces the same results as that would have been obtained with a 34.3 keV monoenergetic X-ray source. Rather, it is a phenomenological observation that at least one set of linear attenuation coefficients of the inspected material phases happen to have a linear relationship with the polychromatic tomography's GSVs. Once the observation is made, the GSVs can be used to evaluate the mass density of the inspected material phases.

The linear relationship shown in Figure 2b can be expressed in the generalized form

$$GSV(\vec{r}, E) = \sum_i^n C_1 \mu_i(\rho, V, Z, E, \vec{r}) + C_2 \quad (3)$$

In the current case of 60 kV acceleration voltage and 200 μA tube current,  $C_1 = 0.121$  and  $C_2 = 0.00362$ . Though deviating from the form of eq 2 by a constant  $C_2$ ,  $C_2$  is comparably small and most likely reflects reproducible influences caused by tomographic artifacts (e.g., beam hardening) or by X-ray flux departure from the flat-field correction during a scan and can thus be mitigated or subtracted.

**Image Acquisition and Quantification Workflow.** Tomographic scans for one image series need to be performed with fixed X-ray parameters, as described in the Experimental Section to ensure that the grayscale values are constant for the same material phases (e.g., PEEK, air, and water). To quantify the liquid water in the porous structure, both a “dry scan” and a “wet scan” are required. In the wet scan, the increased X-ray attenuation by the water (replacing

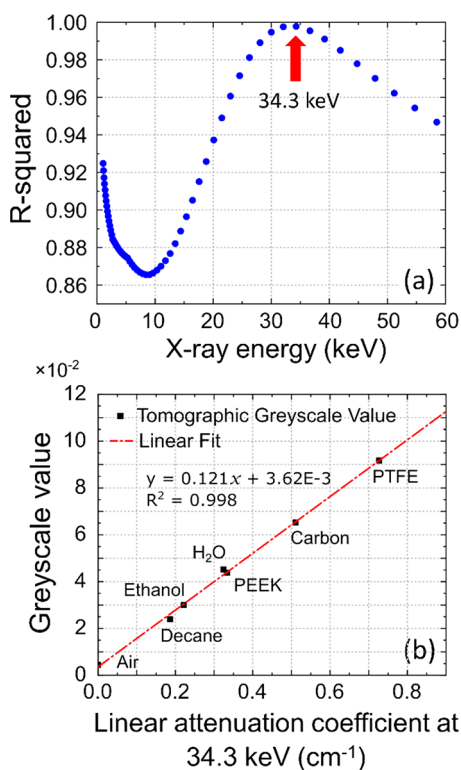


**Figure 2.** Correlation of the experimental grayscale values with the X-ray attenuation coefficients. (a)  $R^2$  values for the linear curve fit of the grayscale value vs attenuation coefficient correlation of materials shown in (b) between 1 and 60 keV X-ray energy; (b) grayscale value vs attenuation coefficient plot at the energy of the best fit (34.3 keV).

the air in the pores) manifests itself as a higher grayscale value at the voxels where the liquid appears. As the GSV increases linearly with the amount of water in the pores, by voxel-to-voxel subtraction, the obtained difference in the grayscale value is directly proportional to the amount of liquid existent in the pore structure. Image alignment is carried out in 3Dslicer<sup>48</sup> using the rigid registration function. The resultant image is called the “difference image”,  $GSV_{\text{diff img}}$ .

$$GSV_{\text{diff img}}(\vec{r}) = C_l \mu_{\text{liquid}}(\vec{r}) \quad (4)$$

When there is freestanding liquid (droplets or pools) in the difference image, its average grayscale value ( $\overline{GSV}_{\text{pool in diff img}}$ ) can serve as the normalization factor from which the relative volume fraction of the liquid at each voxel of the difference image is obtained (assuming isothermal experimental conditions):

$$\frac{GSV_{\text{diff img}}(\vec{r})}{\overline{GSV}_{\text{pool in diff img}}} = \frac{\mu_{\text{liquid}}(\vec{r})}{\mu_{100\% \text{ liquid}}} = LVF(\vec{r}) \text{ (isothermal condition)} \quad (5)$$

LVF stands for liquid volume fraction, the relative amount of the liquid present in the voxel with respect to the voxel volume.

**Porosity and Saturation Mapping.** When the medium is fully saturated by the wetting liquid, the liquid volume fraction ( $LVF_{\text{sat}}(\vec{r})$ ) equals the porous medium’s open porosity,  $\varepsilon(\vec{r})$ .

$$\varepsilon(\vec{r}) = \frac{V_{\text{open pores}}(\vec{r})}{V_{\text{voxel}}} = \frac{V_{\text{saturating liquid}}(\vec{r})}{V_{\text{voxel}}} = LVF_{\text{sat}}(\vec{r}) \quad (6)$$

Equation 6 provides a convenient way to map the spatial porosity distribution of a porous medium independent of the composition and pore size distribution (porosity imaging).

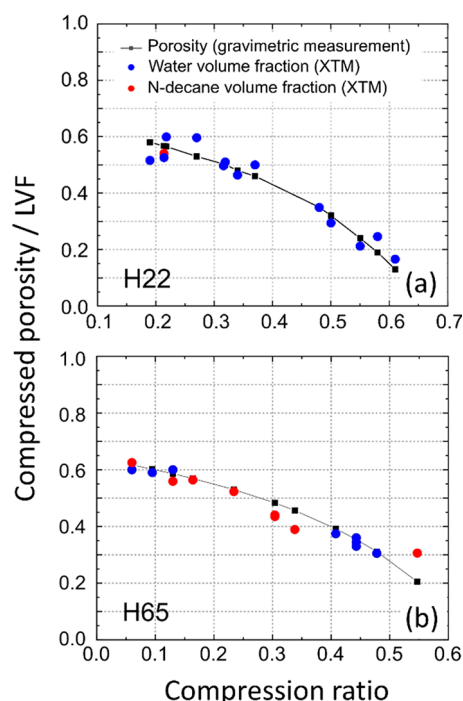


**Figure 3.** Validation of porosity imaging using eq 6 for (a) H22 and (b) H65; black squares and line: gravimetrically determined porosity at different compression ratios; blue dots: water as wetting liquid; red dots: *n*-decane as wetting liquid.

The validation of eq 6 is provided in Figure 3. H22 and H65 were compressed at a variety of compressions and fully saturated. By tomographic imaging, the  $LVF_{\text{sat}}(\vec{r})$  is obtained for both saturated materials and compared to the corresponding compressed porosity  $\varepsilon(\vec{r})$  predicted by eq 1 according to the initial porosity and compression ratio. The results for H22 (Figure 3a) and H65 (Figure 3b) show agreement between the image-derived  $\overline{LVF}_{\text{sat}}$  (averaged across an area; see Section S1.2) and the weight-determined compressed porosity  $\bar{\varepsilon}$ , validating eq 6. As seen in Figure 3, eq 6 is valid using polychromatic XTM regardless of the pore size distribution of the porous material of choice and the wetting liquid used. It concludes the applicability of the imaging method for porosity mapping.

Once the porosity image and the LVF distribution are obtained, the saturation map can be calculated using the combination of both.

$$\frac{LVF(\vec{r})}{\varepsilon(\vec{r})} = \text{saturation}(\vec{r}) \quad (7)$$

Here, saturation is defined as the liquid volume fraction in the pore space of a porous material.

**Postprocessing.** The intruded GDL fibers in the MPL difference image are first excluded by thresholding and assigning NaN (not a number) to these voxels. Then, the ImageJ process “3D mean filtering”<sup>19</sup> using a radius of 5 voxels is applied to lower the image noise. It is chosen because the filter is quantitative and isotropic and sacrifices the image resolution less than, e.g., image binning. For thin materials (e.g., <5 slices), 2D instead of 3D mean filtering with a 5 voxel radius was used to prevent filtered voxel values from being affected by neighboring interfacial (non-MPL) voxels. The radius of the mean filter was chosen as the best compromise between noise reduction and image feature preservation. The image noise ( $\sigma_{\text{noise}}$ , error) was obtained by measuring the standard deviation of the grayscale values of the voxels belonging to the liquid pool in the difference image. Since here the X-ray attenuation is constant, the fluctuation of the grayscale values directly reflects the noise. The image noise was determined to follow a near-Gaussian distribution

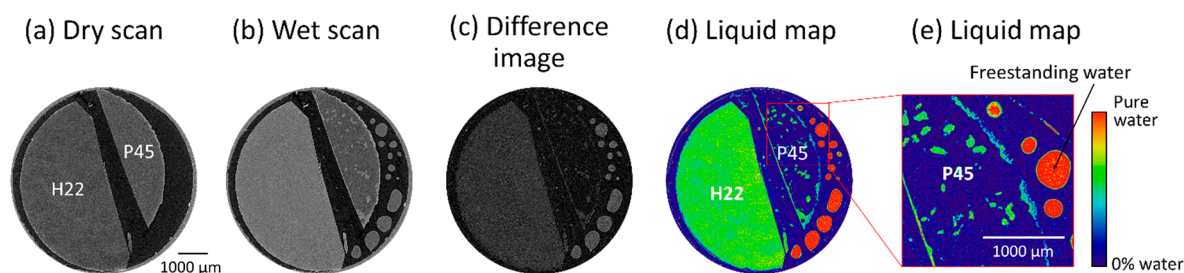


**Figure 4.** Slice of the tomographic scan of H22 and P45 illustrating the workflow of image acquisition and evaluation: (a) dry scan; (b) wet scan; (c) difference image; (d) colored liquid map; (e) enlarged selected region of P45; voxel edge length:  $2.5 \mu\text{m}$ .

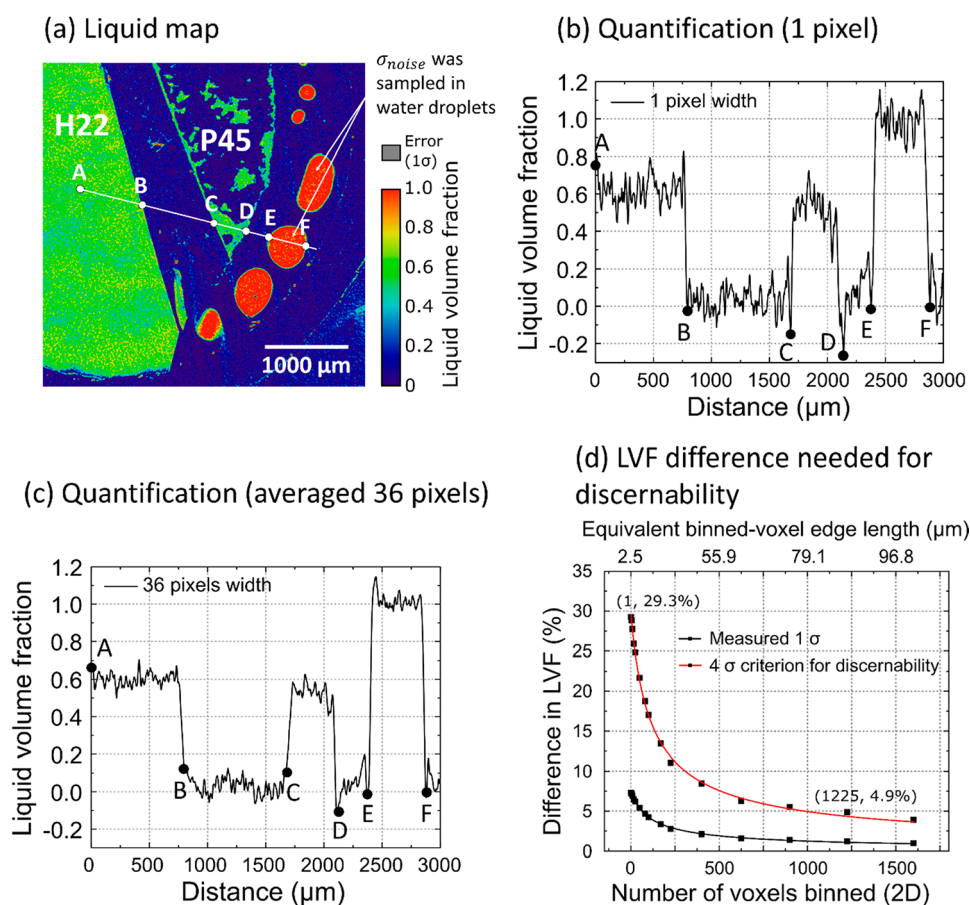


**Figure 5.** Quantification of selected water clusters in P45. (a) Water map with color code and error bar showing each image voxel evaluation's standard deviation; (b) numeric LVF profile across the line drawn in the water map with a one pixel line width; (c) numeric LVF profile with a 36 pixel line width; (d)  $4\sigma$  criterion for discernability of LVF with respect to the numbers of voxels binned; voxel edge length:  $2.5 \mu\text{m}$ .

and was found to be homogeneous across the tomogram, where no sharp phase boundary occurs (e.g., the sample chamber's floor). As a result, the tomographic slices close to the material boundaries are not analyzed.

In the figures,  $\sigma_{\text{noise}}$  is presented in terms of the degree to which it affects the LVF evaluation at each voxel; i.e., the error bar given is equal to  $\sigma_{\text{noise}}/\sqrt{GSV_{\text{water}}}$ . For the figures, a  $1\sigma$  error bar is provided for the ease of voxel-to-voxel LVF comparison. Other error criteria are mentioned in separate discussions.

## RESULTS AND DISCUSSION

The morphology, pore size distribution, and density of the MPLs depend on the composition, in particular the carbon material, as well as on the manufacturing process such as ink composition and additives.<sup>15</sup> Furthermore, the structural information on the MPL of commercial GDLs is not well-

documented. The MPLs can therefore generally not be used as materials for straightforward methodology validation. Porous model materials (H22, P45, H65), yielded with compression and being structurally homogeneous, were consequently chosen to demonstrate the applicability of the imaging method for various materials and processes first. The first part of the results and discussion validates and establishes the limits for the tomographic image evaluation method using these model materials. On the basis of this verification, the porosity image of a commercial MPL and an in-house made MPL is presented. Finally, when the porosity and liquid volume fraction (LVF) evaluation procedures are combined, the saturation evaluation of an easily wetted MPL is provided, concluding the validity of the method for fuel cell imaging applications.

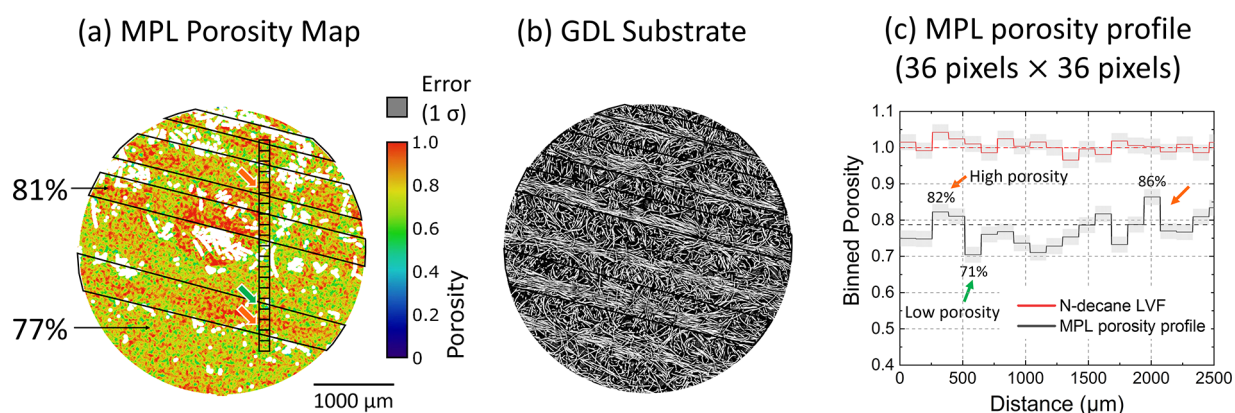


**Figure 6.** Porosity distribution of one tomographic slice of the MPL located near the interface toward the GDL of the Li100/H14. (a) MPL porosity map with tilted black enclosures marking the higher-porosity regions and the vertical series of small boxes ( $36 \text{ pixels} \times 36 \text{ pixels}$  each) marking the porosity profile measurement region; GDL fibers are excluded and colored white. (b) Tomographic slice of the H14 GDL directly next to the MPL; the tilted enclosures indicate the same regions as in (a). (c) Illustration of the MPL imaged porosity variation (black line) as compared to the imaged *n*-decane LVF variation in the *n*-decane pool (red line); the  $\pm 1\sigma$  error for every  $36 \text{ pixels} \times 36 \text{ pixels}$  averaged measurement is illustrated by the gray shading; voxel edge length:  $3.6 \mu\text{m}$

**Method Validation via Model Materials.** The X-ray tomographic imaging results for the wetted, unresolved porous structure can be analyzed by the change of grayscale values, as shown in Figure 4. The image series summarizes the image acquisition pipeline with all evaluation steps. Here, model materials of choice are H22 (left, hydrophilic) and P45 (right, hydrophobic) first imaged in the dry state (Figure 4a). For the wet scan (Figure 4b), water was manually injected from the bottom bore (below H22) until excessive water was seen outside the model materials and the whole setup was left at rest for 38 h before the scan started to allow condensation to take place in the P45.

The change in grayscale is well observable for the water-filled H22 material; the condensation of water in the hydrophobic P45 is also visible (Figure 4b). For quantification, the water is represented first in the difference image (Figure 4c); then, a color-coded liquid map is derived using the freestanding water at the edge of the field of view as the quantification reference (Figures 4d,e).

In the liquid map, the regions with no water and pure water are clearly identifiable. The water in the model material pores manifests with a concentration in between the absence and the total occupation of water.

For the quantitative interpretation of the liquid map, the lower part of P45 is used (Figure 5a), where a straight line can be drawn across the hydrophilic H22 material, water clusters in P45, and the water droplets. The color code shows that H22 and P45 have a liquid volume fraction (LVF) lower than one, as expected. It is because water only fills the pore space of the polymer filters. The imaged LVF in H22 is 58% overall, showing that H22 is saturated, as its actual compressed porosity, determined according to eq 1, is  $58 \pm 1.8\%$ .

The liquid map has a  $1\sigma$  error equivalent of 7.8% LVF. It is illustrated by the error bar on top of the color code in Figure 5a. With the  $1\sigma$  LVF error, at each voxel of the liquid map, the tomography-derived LVF has a 68% chance to lie within the interval [physical LVF  $- \sigma$ , physical LVF  $+ \sigma$ ]. Here, the “physical LVF” is the volume fraction of liquid that physically exists in the porous medium at that voxel. It is seen that, while the accuracy of the tomographic image evaluation is restricted by the image artifacts and the linearity shown in Figure 2, the precision of the LVF spatial evaluation is determined by the

image noise, leading to the probabilistic nature of image interpretation.

An efficient way to narrow down the confidence interval for determining physical LVF is to merge multiple image voxels and obtain an average LVF representing the merged voxels (binned voxels). On a bigger scale (effectively lowering the spatial resolution), the averaged imaged LVF values become more accurate due to statistically reduced noise. As mentioned in Figure 5b, the numeric profile of the imaged LVF across the straight line drawn in Figure 5a with one pixel line width has a standard deviation of  $\pm 7.8\%$  LVF. However, when the line has 36 pixels in thickness (18 pixels on each side), each distance increment along the line is characterized by a lower standard deviation of  $\pm 2.5\%$  LVF (Figure 5c) due to averaging. With the noise-reduced profile, it can be assessed that the line segment  $\overline{AB}$  shows ca. 60% of LVF in one tomographic slice of H22, whereas  $\overline{CD}$  indicates that the LVF in P45 along the path is varying between 40% and 60%.

The decreasing image random noise ( $1\sigma$ ) with respect to the increasing number of binned (merged) voxels is plotted in Figure 5d.  $4\sigma$  is also drawn as a criterion to compare larger examination regions. It is chosen so that, when two imaged LVF measurements differ by more than  $4\sigma$  LVF, we have a 99.5% confidence level that these two measurements result from a distinct difference in the physical LVF. Figure 5d thus describes the trade-off between the interpretable image resolution and the gained confidence in image quantification. As a result, for every  $35 \text{ pixels} \times 35 \text{ pixels}$  ( $87.5 \mu\text{m} \times 87.5 \mu\text{m}$ ) area in the 2D tomographic slice of Figure 5a (1225 voxels binned), any measured average LVF difference of more than 4.9% ( $4\sigma$ ) from one another can be determined to be the result of the difference in the actual amount of water existing in the porous materials. Furthermore, the curve for  $4\sigma$  discernability (Figure 5d) predicts that the measurement of  $\overline{\text{GSV}}_{\text{water}}$  used to translate grayscale values to LVF is highly precise. With a typically large measurement sample population, the error is negligible, therefore not included in the image evaluation calculation. For example, 618 045 voxels were sampled for  $\overline{\text{GSV}}_{\text{water}}$  in the case for Figures 4 and 5, giving only  $\pm 0.3\%$  LVF uncertainty ( $4\sigma$ ) based on the extrapolation of the  $4\sigma$  curve in Figure 5d.

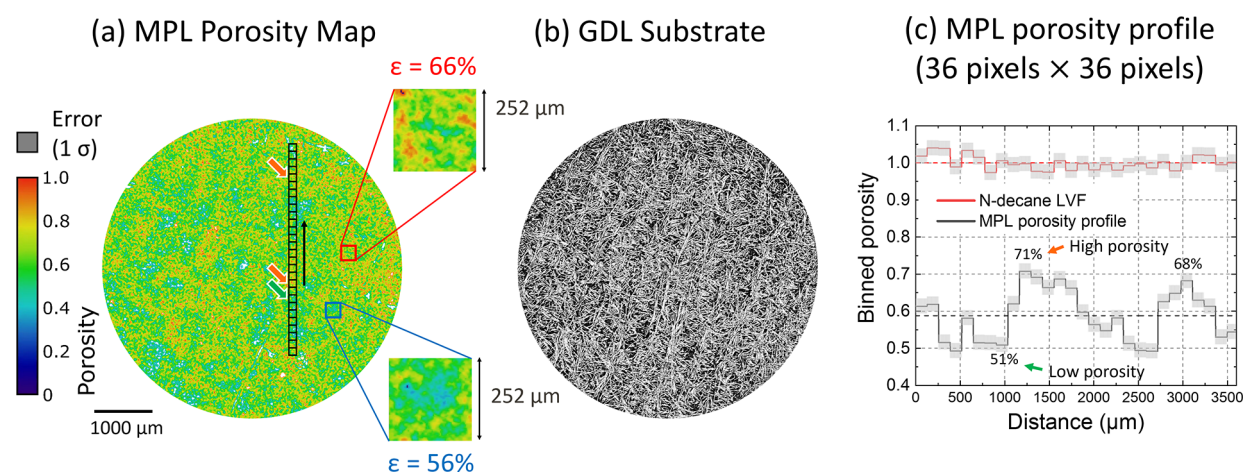


**Figure 7.** Porosity distribution of one tomographic slice of the MPL of the Freudenberg H23C6 GDL. (a) MPL porosity map with the vertical series of small boxes (36 pixels  $\times$  36 pixels each) marking the porosity profile measurement regions; non-MPL structures are excluded and shown in white. (b) The GDL substrate under the MPL. (c) 36 pixels  $\times$  36 pixels-averaged MPL porosity profile (black line) with respect to the distance from the first bottom black box in (a); the imaged *n*-decane LVF variation in the *n*-decane pool is plotted by the red line; the  $\pm 1\sigma$  error for every 36 pixels  $\times$  36 pixels average measurement is illustrated by the gray shading; voxel edge length: 3.6  $\mu\text{m}$ .

**Porosity Imaging of MPLs.** As shown in eq 6, the image of an MPL with a wetting liquid can provide its porosity distribution. The porosity image of the Li100/H14 MPL demonstrates a total average porosity of 79% for the imaged slice (thickness = 3.6  $\mu\text{m}$ ) shown in Figure 6a. The diameter of the circular disk is 3.6 mm, and the porosity distribution is indicated by the color code with 9.2% voxel-to-voxel uncertainty.

Independently, Simon et al.<sup>44</sup> had determined the overall porosity of the same (freestanding) Li100 MPL to be 79% and 80% (by mercury intrusion porosimetry (MIP) and weighing, respectively). The close agreement between the imaging result and their measurements confirms the accuracy of the imaging method.

The MPL porosity map in Figure 6a shows that the Li100/H14 MPL has an uneven porosity distribution, unlike the largely homogeneous model materials (e.g., H22). The Li100 MPL on H14 has higher porosity domains distributed in a specific stripe pattern. The pattern is likely influenced by the underlying GDL substrate (Figure 6b), as the spatial occurrence of the higher-porosity regions coincides with the densely entangled carbon fibers in the H14 substrate (marked in tilted black enclosures in Figure 6a,b). A through-plane tomographic image of the Li100/H14 is provided in Figure S2 for illustration. The average porosity of the higher-porosity region is 81% with  $4\sigma$  uncertainty of  $\pm 0.84\%$  extrapolated from the  $4\sigma$  discernability curve for this image volume (not shown here), whereas the lower-porosity region of MPL is  $77 \pm 0.68\%$  ( $4\sigma$ ). The error is estimated from the GSV fluctuation within the liquid pool with respect to a certain sampling size. With the average porosity difference in the two domains being larger than the  $4\sigma$  error resulting from the image noise, the porosity difference in the two regions is thus concluded to be physical.

The inhomogeneity of the MPL porosity is also quantitatively examined as a porosity profile. Figure 6c plots the average porosity of every 36 pixels  $\times$  36 pixels (129.6  $\mu\text{m}$   $\times$  129.6  $\mu\text{m}$ ) square area on the *y*-axis (through-plane thickness = 1 voxel), and it changes corresponding to the relative distance traveled by the series of the squares starting from the bottom square plotted in Figure 6a.  $4\sigma$  for each square-volume

measurement is 8.7% (estimated from the liquid pool, not shown here), meaning that any porosity measurements separated by 8.7% or above reflect the physical porosity difference (the chance of them resulting from the same physical LVF is  $<0.5\%$ ). As a result, the lower-porosity (71%) region plotted in Figure 6c at about a 600  $\mu\text{m}$  distance from the origin (bottom square) and the higher-porosity (82%) region at about 300  $\mu\text{m}$  have different physical porosities.

For comparison, the LVF profile of the *n*-decane sampled at the liquid pool of the same difference image volume is plotted in Figure 6c. Here, the variation of LVF comes purely from image noise. Even though there is no  $>8.7\%$  LVF difference across the examined area of the *n*-decane pool, as much as a 7.7% LVF difference is present ( $\sim 3.5\sigma$ , corresponding to 1.2% probability of occurrence), showing the error and the limit of the evaluation as a result of the image noise.

The commercial MPL on the “Freudenberg H23C6” gas diffusion layer provides a different spatial porosity distribution than Li100/H14, as shown in Figure 7a. The MPL of the Freudenberg H23C6 GDL has a generally lower porosity (62%), and just like the MPL on Li100/H14, the porosity distribution is not even; it also does not show a clear regular pattern. When square areas of a higher-porosity region (red square in Figure 7a) and a lower-porosity region (blue square) are each sampled and have the dimensions of 70 pixels  $\times$  70 pixels or 252  $\mu\text{m}$   $\times$  252  $\mu\text{m}$ , the  $4\sigma$  discernability derived from the liquid pool is 5.0%. This means, to be able to confidently tell that any porosity difference of  $\geq 5.0\%$  porosity results from a physical porosity difference with a confidence level of 99.5%, we have to compare between averaged porosity values of regions  $\geq 252 \mu\text{m} \times 252 \mu\text{m}$  in area. Similarly, if we would like to compare among smaller regions (36 pixels  $\times$  36 pixels or 130  $\mu\text{m}$   $\times$  130  $\mu\text{m}$ ), thus gaining interpretable image resolution, the porosity discernability will be reduced to 7.6% ( $4\sigma$ ). Any porosity difference among regions of 130  $\mu\text{m}$   $\times$  130  $\mu\text{m}$  in dimension lower than 7.6% cannot be determined to be the reflection of the physical porosity difference in the MPL with a 99.5% confidence level.

The 36 pixels  $\times$  36 pixels-averaged porosity profile of the MPL is plotted in Figure 7c. For comparison, the LVF profile of the *n*-decane pool is shown too (red line). With

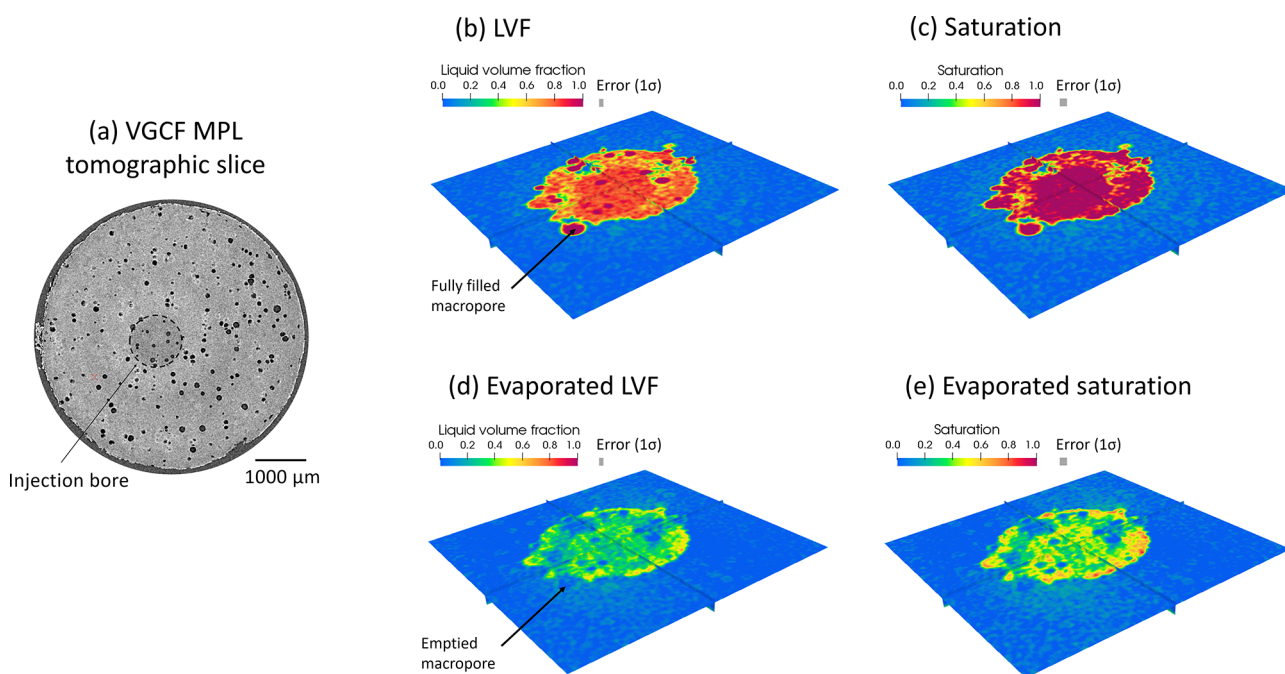


**Figure 8.** 3D saturation image of the VGCF MPL after liquid water injection (view from the top): (a) dry in-plane MPL structure; (b, c) liquid volume fraction and saturation at the identical region above the injection bore after water injection; (d, e) corresponding LVF and saturation image after 20 h of room temperature evaporation. Voxel edge length:  $3.6 \mu\text{m}$ .

discernability being  $7.6\%$  ( $4\sigma$ ) in porosity, it is confirmed that the low-porosity region ( $51\%$ ) at ca.  $900 \mu\text{m}$  from the origin (bottom black square in Figure 7a) and the high-porosity region ( $71\%$ ) at ca.  $1200 \mu\text{m}$  have different physical porosities, verifying that the MPL is inhomogeneous in porosity.

The XTM image of the GDL substrate close to the MPL is provided in Figure 7b for reference. SEM and XTM images of the MPL of the H23C6 GDL in the dry state as well as the visualization of the porosity map in a 3D surface plot (for better visualization of image noise) are given for reference in Figures S5 and S6.

The analyses demonstrated here have used only one in-plane slice of the MPL that is close to the center for lucidity. The entire MPL volume can be visualized via the same workflow. The analyses show that the MPL morphology, also for commercial materials, cannot be treated as homogeneous, and for quantitative evaluation of saturation, the porosity distribution determination must precede.

**Saturation Imaging of Water in the MPL.** With the defined limits and precision of the tomographic imaging described in the previous sections, the VGCF MPL on the H14 substrate (VGCF/H14) is characterized for its liquid water saturation distribution after water injection at room temperature.

To obtain the water saturation map, the porosity was first obtained with ethanol as the wetting liquid (see procedure in the Experimental Section). The obtained porosity image is shown in Figure S4. After being dried, water is injected to obtain the LVF of water (Figure 8b,d), which is easily possible as a significant fraction of the pore size of the VGCF MPL is  $>1 \mu\text{m}$  (see Figure S3c), enabling facile water injection. The saturation map is then obtained by dividing the LVF by the porosity according to eq 7. The results are shown in Figure 8.

One in-plane slice of the VGCF MPL is visualized in Figure 8a. This slice, showing the relative position of the injection bore, is located  $43 \mu\text{m}$  away from the H14 substrate, well

within the VGCF MPL (total VGCF MPL thickness =  $140 \mu\text{m}$ ; this is an increased thickness for imaging purposes compared to the application in fuel cells). In the dry tomogram, the central region (above the injection bore) has a slightly lower GSV than the MPL outside due to lower compression.

After manual water injection, the water is confined to the region directly above the water injection bore due to the hydrophobicity of the MPL (Figure 8b). The liquid volume fraction of the MPL in the horizontal slice in Figure 8b is generally equal to  $0.8$  in the unresolved MPL pores with low-LVF domains toward the periphery of the circular region and several fully filled macropores. The macropores are a distinct feature of this VGCF MPL of increased thickness (also shown in the dry tomogram), whose diameters are ca.  $100 \mu\text{m}$  in the in-plane direction, and their shapes are fully resolvable by the tomographic imaging. For the LVF images in Figure 8, the  $1\sigma$  error from voxel to voxel is  $3\%$  LVF after (3D) filtering. Here, 3D filtering is possible due to the increased MPL thickness.

The saturation image (Figure 8c) shows that, despite having a LVF lower than 1, most of the wetted, unresolved pores of the MPL are fully saturated, having the same degree of saturation as the fully filled macropores. The implication is that such regions would not be available for the gas transport pathways during fuel cell operation. On the other hand, the spatially-dependent difference between the LVF and the saturation image is a result of local porosity variation. The porosity distribution for the same slice as in Figure 8a is provided in Figure S4.

After 20 h of room temperature evaporation, the LVF (Figure 8d) and saturation distribution (Figure 8e) have accordingly lower values. The LVF is generally reduced everywhere with some of the previously fully wetted macropores now empty. The trend is that the LVF remains slightly higher toward the boundary of the circular wet domain. The distribution of saturation reported in Figure 8e shows several

saturation “hot spots” with ca. 70% of saturation spread around the periphery of the wet domain, where the saturation is generally higher, up to 94%. Compared to the LVF, saturation is more inhomogeneous due to the sensitivity to the local MPL structure (porosity) variation. The error on a single voxel basis for the saturation maps (Figure 8c,e) is 5% saturation, higher than the LVF images due to error propagation in the image calculation.

Overall, the results show that this workflow based on polychromatic X-ray tomographic imaging, combining LVF and saturation images, provides a quantitative multiphase structural description without the requirement of monochromatic radiation or any a priori knowledge of the MPL structure or composition. The presented methodology is compatible with steady-state fuel cell operation (stabilized water distribution) and can be applied for the analysis of operando experiments,<sup>49</sup> paving the way for studying water saturation in MPLs during operation.

## CONCLUSION

An X-ray tomographic imaging methodology is presented and validated that allows for the quantification of liquid in the unresolved pores of nanopore materials with a polychromatic X-ray source. Using a laboratory CT scanner, the method is validated using model materials and is shown to be able to quantitatively characterize the spatial variation of porosity and water sorption properties of microporous layer (MPL) materials for polymer electrolyte fuel cells.

While not able to provide the explicit 3D MPL porous structure (as achieved by high-resolution electron microscopy techniques or X-ray nanotomography), the XTM method with voxel sizes in the micrometer range benefits from the larger field of view and being able to characterize material and liquid sorption inhomogeneities over a scale of a few millimeters. Variation of the MPL porosity at this scale is indeed observed also for commercial materials and is expected to influence the water transport during fuel cell operation. The XTM method presented here thus bridges the scales between the MPL microstructure determination and the water transport characterization in fuel cells. Another advantage of the XTM method is the ability to obtain the spatial distributions of the porosity and liquid volume fraction in the MPLs without a priori knowledge of the material's structure or composition.

The method is demonstrated here in an ex situ setup but provides the path forward to characterize the saturation properties of the MPLs also under fuel cell operando conditions. Here, local MPL saturation plays a key role in modulating the water distribution in other fuel cell components, strongly influencing the local fuel cell performance. Owing to the compatibility with most conventional MPLs, the method can be applied to various types of GDLs with a microporous layer to determine the influence of the microporous layer on fuel cell performance.

Using a laboratory CT scanner for the presented results, the time resolution of the technique is 1–2 h. In the future, the method development can be transferred to synchrotron-based operando XTM imaging for time resolutions on the second scale with the aim for characterization of dynamic water sorption or evaporation processes in the MPL.

## ASSOCIATED CONTENT

### Supporting Information

The Supporting Information is available free of charge at <https://pubs.acs.org/doi/10.1021/acsami.0c22358>.

Model material initial porosity measurement, compressed model material thickness measurement, high-resolution tomographic image of the Li100/H14 gas diffusion layer, pore size distribution of the VGCF MPL, porosity distribution of the VGCF MPL, additional images of the MPL from the commercial Freudenberg H23C6 gas diffusion layer (PDF)

## AUTHOR INFORMATION

### Corresponding Author

Felix N. Büchi – *Electrochemistry Laboratory, Paul Scherrer Institute, Villigen CH-5232, Switzerland*; [orcid.org/0000-0002-3541-4591](https://orcid.org/0000-0002-3541-4591); Email: [felix.buechi@psi.ch](mailto:felix.buechi@psi.ch)

### Authors

Yen-Chun Chen – *Electrochemistry Laboratory, Paul Scherrer Institute, Villigen CH-5232, Switzerland*

Anne Berger – *Chair of Technical Electrochemistry, Department of Chemistry and Catalysis Research Center, Technical University of Munich, Garching D-85748, Germany*

Salvatore De Angelis – *Electrochemistry Laboratory, Paul Scherrer Institute, Villigen CH-5232, Switzerland*

Tobias Schuler – *Electrochemistry Laboratory, Paul Scherrer Institute, Villigen CH-5232, Switzerland*

Michele Bozzetti – *Institute of Materials, Ecole Polytechnique Federale de Lausanne (EPFL), Lausanne CH-1015, Switzerland*

Jens Eller – *Electrochemistry Laboratory, Paul Scherrer Institute, Villigen CH-5232, Switzerland*; [orcid.org/0000-0002-9348-984X](https://orcid.org/0000-0002-9348-984X)

Vasiliki Tileli – *Institute of Materials, Ecole Polytechnique Federale de Lausanne (EPFL), Lausanne CH-1015, Switzerland*; [orcid.org/0000-0002-0520-6900](https://orcid.org/0000-0002-0520-6900)

Thomas J. Schmidt – *Electrochemistry Laboratory, Paul Scherrer Institute, Villigen CH-5232, Switzerland*; *Laboratory of Physical Chemistry, ETH Zürich, Zürich CH-8093, Switzerland*; [orcid.org/0000-0002-1636-367X](https://orcid.org/0000-0002-1636-367X)

Complete contact information is available at: <https://pubs.acs.org/10.1021/acsami.0c22358>

### Author Contributions

The manuscript was written through contributions of all authors. All authors have given approval to the final version of the manuscript.

### Funding

All the authors gratefully acknowledge funding from the Swiss National Science Foundation, under the funding scheme Sinergia (project grant number 180335).

### Notes

The authors declare no competing financial interest.

## ACKNOWLEDGMENTS

We would like to thank H. Gasteiger (TU Munich) for insightful discussions and Christoph Csoklich and Adrian Mularczyk (both PSI) for technical assistance. We acknowledge the Paul Scherrer Institut, Villigen, Switzerland for

provision of synchrotron radiation beamtime at the TOMCAT beamline X02DA of the SLS and would like to thank Federica Marone for assistance.

## REFERENCES

- (1) IEA CO<sub>2</sub> Emissions from Fuel Combustion 2019; IEA, 2019; <https://webstore.iea.org/co2-emissions-from-fuel-combustion-2019-highlights>.
- (2) O'Malley, M. J.; Anwar, M. B.; Heinen, S.; Kober, T.; McCalley, J.; McPherson, M.; Muratori, M.; Orths, A.; Ruth, M.; Schmidt, T. J.; Tuohy, A. Multicarrier Energy Systems: Shaping Our Energy Future. *Proc. IEEE* **2020**, *108* (9), 1437–1456.
- (3) Rosen, M. A.; Koochi-Fayegh, S. The Prospects for Hydrogen as an Energy Carrier: An Overview of Hydrogen Energy and Hydrogen Energy Systems. *Energy, Ecol. Environ.* **2016**, *1* (1), 10–29.
- (4) Hoogers, G., Ed. 4.1: General Design Features. In *Fuel Cell Technology Handbook*; CRC Press: Boca Raton, FL, 2003; pp 4.1–4.28.
- (5) Chen, J.; Matsuura, T.; Hori, M. Novel Gas Diffusion Layer with Water Management Function for PEMFC. *J. Power Sources* **2004**, *131* (1–2), 155–161.
- (6) Dai, W.; Wang, H.; Yuan, X. Z.; Martin, J. J.; Yang, D.; Qiao, J.; Ma, J. A Review on Water Balance in the Membrane Electrode Assembly of Proton Exchange Membrane Fuel Cells. *Int. J. Hydrogen Energy* **2009**, *34* (23), 9461–9478.
- (7) Qi, Z.; Kaufman, A. Improvement of Water Management by a Microporous Sublayer for PEM Fuel Cells. *J. Power Sources* **2002**, *109* (1), 38–46.
- (8) Antolini, E.; Passos, R. R.; Ticianelli, E. A. Effects of the Cathode Gas Diffusion Layer Characteristics on the Performance of Polymer Electrolyte Fuel Cells. *J. Appl. Electrochem.* **2002**, *32* (4), 383–388.
- (9) Paganin, V. A.; Ticianelli, E. A.; Gonzalez, E. R. Development and Electrochemical Studies of Gas Diffusion Electrodes for Polymer Electrolyte Fuel Cells. *J. Appl. Electrochem.* **1996**, *26*, 297–304.
- (10) Jordan, L. R.; Shukla, A. K.; Behrsing, T.; Avery, N. R.; Muddle, B. C.; Forsyth, M. Diffusion Layer Parameters Influencing Optimal Fuel Cell Performance. *J. Power Sources* **2000**, *86* (1), 250–254.
- (11) Park, G. G.; Sohn, Y. J.; Yang, T. H.; Yoon, Y. G.; Lee, W. Y.; Kim, C. S. Effect of PTFE Contents in the Gas Diffusion Media on the Performance of PEMFC. *J. Power Sources* **2004**, *131* (1–2), 182–187.
- (12) Park, S. B.; Park, Y. I. Fabrication of Gas Diffusion Layer (GDL) Containing Microporous Layer Using Flourinated Ethylene Propylene (FEP) for Proton Exchange Membrane Fuel Cell (PEMFC). *Int. J. Precis. Eng. Manuf.* **2012**, *13* (7), 1145–1151.
- (13) Latorrata, S.; Gallo Stampino, P.; Cristiani, C.; Dotelli, G. Novel Superhydrophobic Microporous Layers for Enhanced Performance and Efficient Water Management in PEM Fuel Cells. *Int. J. Hydrogen Energy* **2014**, *39* (10), 5350–5357.
- (14) Zhou, J.; Shukla, S.; Putz, A.; Secanell, M. Analysis of the Role of the Microporous Layer in Improving Polymer Electrolyte Fuel Cell Performance. *Electrochim. Acta* **2018**, *268*, 366–382.
- (15) Nagai, Y.; Eller, J.; Hatanaka, T.; Yamaguchi, S.; Kato, S.; Kato, A.; Marone, F.; Xu, H.; Büchi, F. N. Improving Water Management in Fuel Cells through Microporous Layer Modifications: Fast Operando Tomographic Imaging of Liquid Water. *J. Power Sources* **2019**, *435* (March), 226809.
- (16) Tabe, Y.; Aoyama, Y.; Kadowaki, K.; Suzuki, K.; Chikahisa, T. Impact of Micro-Porous Layer on Liquid Water Distribution at the Catalyst Layer Interface and Cell Performance in a Polymer Electrolyte Membrane Fuel Cell. *J. Power Sources* **2015**, *287*, 422–430.
- (17) Lee, J.; Hinebaugh, J.; Bazylak, A. Synchrotron X-Ray Radiographic Investigations of Liquid Water Transport Behavior in a PEMFC with MPL-Coated GDLs. *J. Power Sources* **2013**, *227*, 123–130.
- (18) Kannan, A. M.; Menghal, A.; Barsukov, I. V. Gas Diffusion Layer Using a New Type of Graphitized Nano-Carbon PURE-BLACK® for Proton Exchange Membrane Fuel Cells. *Electrochem. Commun.* **2006**, *8* (5), 887–891.
- (19) Manzi-Orezzoli, V.; Siegwart, M.; Scheuble, D.; Chen, Y.; Schmidt, T. J.; Boillat, P. Impact of the Microporous Layer on Gas Diffusion Layers with Patterned Wettability I: Material Design and Characterization Impact of the Microporous Layer on Gas Diffusion Layers with Patterned Wettability I: Material Design and Characterization. *J. Electrochem. Soc.* **2020**, *167*, 064516.
- (20) Deevanhay, P.; Sasabe, T.; Tsushima, S.; Hirai, S. Effect of Liquid Water Distribution in Gas Diffusion Media with and without Microporous Layer on PEM Fuel Cell Performance. *Electrochem. Commun.* **2013**, *34*, 239–241.
- (21) Oberholzer, P.; Boillat, P.; Siegrist, R.; Kästner, A.; Lehmann, E. H.; Scherer, G. G.; Wokaun, A. Simultaneous Neutron Imaging of Six Operating PEFCs: Experimental Set-up and Study of the MPL Effect. *Electrochem. Commun.* **2012**, *20* (1), 67–70.
- (22) Owejan, J. P.; Owejan, J. E.; Gu, W.; Trabold, T. A.; Tighe, T. W.; Mathias, M. F. Water Transport Mechanisms in PEMFC Gas Diffusion Layers. *J. Electrochem. Soc.* **2010**, *157* (10), B1456.
- (23) Baghalha, M. The Effect of MPL Permeability on Water Fluxes in PEM Fuel Cells: Experimental Verification. *ECS Trans.* **2011**, *41* (1), 521–538.
- (24) Weber, A. Z.; Newman, J. Effects of Microporous Layers in Polymer Electrolyte Fuel Cells. *J. Electrochem. Soc.* **2005**, *152* (4), A677.
- (25) Wang, X.; Nguyen, T. V. Modeling the Effects of the Cathode Micro-Porous Layer on the Performance of a PEM Fuel Cell. *ECS Trans.* **2009**, *16* (2), 3–12.
- (26) Kim, T.; Lee, S.; Park, H. A Study of Water Transport as a Function of the Micro-Porous Layer Arrangement in PEMFCs. *Int. J. Hydrogen Energy* **2010**, *35* (16), 8631–8643.
- (27) Simon, C.; Endres, J.; Nefzger-Loders, B.; Wilhelm, F.; Gasteiger, H. A. Interaction of Pore Size and Hydrophobicity/Hydrophilicity for Improved Oxygen and Water Transport through Microporous Layers. *J. Electrochem. Soc.* **2019**, *166* (13), F1022–F1035.
- (28) Wong, A.; Bazylak, A. Investigating the Effect of Non-Uniform Microporous Layer Intrusion on Oxygen Transport in Dry and Partially Saturated Polymer Electrolyte Membrane Fuel Cell Gas Diffusion Layers. *ECS Trans.* **2017**, *80* (8), 175–186.
- (29) Nam, J. H.; Lee, K. J.; Hwang, G. S.; Kim, C. J.; Kaviani, M. Microporous Layer for Water Morphology Control in PEMFC. *Int. J. Heat Mass Transfer* **2009**, *52* (11–12), 2779–2791.
- (30) Aoyama, Y.; Suzuki, K.; Tabe, Y.; Chikahisa, T.; Tanuma, T. Water Transport and PEFC Performance with Different Interface Structure between Micro-Porous Layer and Catalyst Layer. *J. Electrochem. Soc.* **2016**, *163* (5), F359–F366.
- (31) Fishman, Z.; Bazylak, A. Heterogeneous Through-Plane Porosity Distributions for Treated PEMFC GDLs. II. Effect of MPL Cracks. *J. Electrochem. Soc.* **2011**, *158* (8), B846.
- (32) Halter, J.; Marone, F.; Schmidt, T. J.; Büchi, F. N. Breaking through the Cracks: On the Mechanism of Phosphoric Acid Migration in High Temperature Polymer Electrolyte Fuel Cells. *J. Electrochem. Soc.* **2018**, *165* (14), F1176–F1183.
- (33) Kato, S.; Yamaguchi, S.; Yoshimune, W.; Matsuoka, Y.; Kato, A.; Nagai, Y.; Suzuki, T. Ex-Situ Visualization of the Wet Domain in the Microporous Layer in a Polymer Electrolyte Fuel Cell by X-Ray Computed Tomography under Water Vapor Supply. *Electrochem. Commun.* **2020**, *111*, 106644.
- (34) Akitomo, F.; Sasabe, T.; Yoshida, T.; Naito, H.; Kawamura, K.; Hirai, S. Investigation of Effects of High Temperature and Pressure on a Polymer Electrolyte Fuel Cell with Polarization Analysis and X-Ray Imaging of Liquid Water. *J. Power Sources* **2019**, *431*, 205–209.
- (35) Alrwashdeh, S. S.; Hausmann, J.; Markötter, H.; Manke, I.; Scholta, J.; Banhart, J.; Göbel, M.; Klages, M. In Operando Quantification of Three-Dimensional Water Distribution in Nanoporous Carbon-Based Layers in Polymer Electrolyte Membrane Fuel Cells. *ACS Nano* **2017**, *11* (6), 5944–5949.

(36) Roth, J.; Eller, J.; Marone, F.; Büchi, F. N. Investigation of the Representative Area of the Water Saturation in Gas Diffusion Layers of Polymer Electrolyte Fuel Cells. *J. Phys. Chem. C* **2013**, *117* (49), 25991–25999.

(37) Eller, J.; Marone, F.; Büchi, F. N. Operando Sub-Second Tomographic Imaging of Water in PEFC Gas Diffusion Layers. *ECS Trans.* **2015**, *69* (17), 523–531.

(38) Eller, J.; Roth, J.; Marone, F.; Stampanoni, M.; Büchi, F. N. Operando Properties of Gas Diffusion Layers: Saturation and Liquid Permeability. *J. Electrochem. Soc.* **2017**, *164* (2), F115–F126.

(39) Xu, H.; Marone, F.; Nagashima, S.; Nguyen, H.; Kishita, K.; Büchi, F. N.; Eller, J. (Invited) Exploring Sub-Second and Sub-Micron X-Ray Tomographic Imaging of Liquid Water in PEFC Gas Diffusion Layers. *ECS Trans.* **2019**, *92* (8), 11–21.

(40) Bühner, M.; Stampanoni, M.; Rochet, X.; Büchi, F.; Eller, J.; Marone, F. High-Numerical-Aperture Macroscopic Optics for Time-Resolved Experiments. *J. Synchrotron Radiat.* **2019**, *26*, 1161–1172.

(41) Eller, J. *X-Ray Tomographic Microscopy of Polymer Electrolyte Fuel Cells*. Ph.D. Dissertation, 2013; <https://doi.org/10.3929/ethz-a-009777184>.

(42) Wang, Y.; Wang, C.-Y. A Nonisothermal, Two-Phase Model for Polymer Electrolyte Fuel Cells. *J. Electrochem. Soc.* **2006**, *153* (6), A1193.

(43) Litster, S.; Djilali, N. Two-Phase Transport in Porous Gas Diffusion Electrodes. *Transp. Phenom. Fuel Cells* **2005**, *1*, 175–213.

(44) Simon, C.; Kartouzian, D.; Müller, D.; Wilhelm, F.; Gasteiger, H. A. Impact of Microporous Layer Pore Properties on Liquid Water Transport in PEM Fuel Cells: Carbon Black Type and Perforation. *J. Electrochem. Soc.* **2017**, *164* (14), F1697–F1711.

(45) White, R. T.; Eberhardt, S. H.; Singh, Y.; Haddow, T.; Dutta, M.; Orfino, F. P.; Kjeang, E. Four-Dimensional Joint Visualization of Electrode Degradation and Liquid Water Distribution inside Operating Polymer Electrolyte Fuel Cells. *Sci. Rep.* **2019**, *9*, 1843.

(46) Chantler, C. T. Theoretical Form Factor, Attenuation, and Scattering Tabulation for  $Z = 1–92$  from  $E = 1–10$  eV to  $E = 0.4–1.0$  MeV. *J. Phys. Chem. Ref. Data* **1995**, *24* (1), 71.

(47) Chantler, C. T. Detailed Tabulation of Atomic Form Factors, Photoelectric Absorption and Scattering Cross Section, and Mass Attenuation Coefficients in the Vicinity of Absorption Edges in the Soft X-Ray ( $Z = 30–36$ ,  $Z = 60–89$ ,  $E = 0.1$  keV–10 keV), Addressing Convergence Issues of Earlier Work. *J. Phys. Chem. Ref. Data* **2000**, *29* (4), 597.

(48) Fedorov, A.; Beichel, R.; Kalpathy-Cramer, J.; Finet, J.; Fillion-Robin, J.-C.; Pujol, S.; Bauer, C.; Jennings, D.; Fennessy, F.; Sonka, M.; Buatti, J.; Aylward, S.; Miller, J. V.; Pieper, S.; Kikinis, R. 3D Slicer as an Image Computing Platform for the Quantitative Imaging Network. *Magn. Reson. Imaging* **2012**, *30* (9), 1323–1341.

(49) Xu, H.; Bühner, M.; Marone, F.; Schmidt, T. J.; Büchi, F. N.; Eller, J. Optimal Image Denoising for In Situ X-Ray Tomographic Microscopy of Liquid Water in Gas Diffusion Layers of Polymer Electrolyte Fuel Cells. *J. Electrochem. Soc.* **2020**, *167* (10), 104505.